Geometry-diversified Coulomb excitations in trilayer AAB stacking graphene

Chiun-Yan Lin,[1] Bor-Luen Huang,[1] Ching-Hong Ho,[2] Godfrey Gumbs,[3,4,*] and Ming-Fa Lin[5,6,†]

[1]*Department of Physics, National Cheng Kung University, 701 Tainan, Taiwan*

[2]*Center of General Studies, National Kaohsiung University of Science and Technology, 811 Kaohsiung, Taiwan*

[3]*Department of Physics and Astronomy, Hunter College of the City University of New York, 695 Park Avenue, New York, New York 10065, USA*

[4]*Donostia International Physics Center (DIPC), P de Manuel Lardizabal, 4, 20018 San Sebastian, Basque Country, Spain*

[5]*Hierarchical Green-Energy Materials Research Center, National Cheng Kung University, 701 Tainan, Taiwan*

[6]*Quantum topology center, National Cheng Kung University, 701 Tainan, Taiwan*

(Received 31 August 2018; revised manuscript received 2 November 2018; published 28 November 2018)

The lower-symmetry trilayer AAB-stacked graphene exhibits rich electronic properties and diverse Coulomb excitations. Three pairs of unusual valence and conduction bands create nine available interband excitations for the undoped case, in which the imaginary (real) part of the polarizability shows one-dimensional square root asymmetric peaks and two-dimensional shoulder structures (pairs of antisymmetric peaks and logarithm-type symmetric peaks). The low-frequency acoustic plasmon, being revealed as a prominent peak in the energy-loss spectrum, can survive in a narrow-gap system with the large density of states from the valence band. This type of plasmon mode is similar to that in a narrow-gap carbon nanotube. However, the decisive mechanism governing this plasmon is the intraband conduction state excitations. Its frequency, intensity and critical momentum exhibit a nonmonotonic dependence on the Fermi energy. The well-defined electron-hole excitation boundaries and the higher frequency optical plasmons are transformed by varying the Fermi energy. Many substantial differences between the electronic properties of AAB and other trilayer graphene stackings are discussed.

DOI: 10.1103/PhysRevB.98.195442

I. INTRODUCTION

Experimental examination of the electronic properties of low-dimensional materials has been scrutinized by using a variety of methods such as angle-resolved photoemission spectroscopy (ARPES) [1–3] and electron energy-loss spectroscopy (EELS) [4–8]. In a remarkable paper, Ohta *et al.* [2] used ARPES to study the Coulomb potential, screening length, and interlayer electronic interactions in multilayer graphene through the comparison with tight-binding calculations. The same technique was also used by Jin *et al.* [3] to determine the thickness-dependence of the electronic band structure of MoS_2. The role played by EELS has been equally impressive. For example, EELS was used to investigate the strain effect on the optical conductivity of graphene [4]. In Ref. [5], high-resolution EELS was used to study the low-energy collective excitations for a Cu(111) surface, which shows a plasmon mode with negative dispersion and an energy of 1.1 eV. This collective mode was suggested to come from the oscillation of electrons constrained into two-dimensional (2D) Shockley surface states on the Cu(111) surface. In the work of Lu *et al.* [8], the plasmon dispersion of epitaxial graphene was measured by using high-resolution EELS. Their results revealed that the π plasmons for single, bilayer, and trilayer graphene (TLG) have significant differences in the in-phase and out-of-phase modes, which arise from different band structures between single- and multilayer graphene.

These aforementioned facts have inspired us to use the tight-binding model to calculate the energy band structure and consequently investigate the behavior of the π electron Coulomb excitations in AAB TLG within the random-phase approximation (RPA). The dependence on the magnitude q and direction ϕ of the transferred momentum $\mathbf{q}$ and the Fermi energy E_F is carefully analyzed. As shown in Fig. 1(a), AAB stacking is a combination of AA and AB stackings. Such a system has been successfully synthesized by reliable methods and investigated, e.g., by using electrostatic-manipulation scanning tunneling microscopy (STM) [9], mechanical exfoliation directly by scalper or scotch tape [10], CVD growth on a SiC substrate [11] and Ru(0001) surface [12], and liquid-phase exfoliation of natural graphite in N-methyl-2-pyrrolidone [13]. From the viewpoint of geometric structure, AAB stacking could be obtained by rotating or horizontal shifting of the first graphene layer of ABA- or ABC-stacked TLG along the armchair direction. That is to say, the stacking configuration is continuously changed under electrostatic modulation of the STM. According to the first-principles method, the ground-state energies for AAA, AAB, ABA, and ABC TLGs are estimated, respectively, as −55.832 866, −55.857 749, −55.862 386, and −55.864 039 eV per unit cell of six carbon atoms [14]. The theoretical calculations predict that the AAB stacking is more stable than the AAA one, or the former with more diversified electronic structure presents the more promising future in experimental syntheses. Unlike other kinds of well-stacked TLGs, the lower-symmetry AAB stacking possesses the most complicated interlayer hopping integrals, which identified from a consistent and detailed comparison between the tight-binding model and

*ggumbs@hunter.cuny.edu
†mflin@mail.ncku.edu.tw

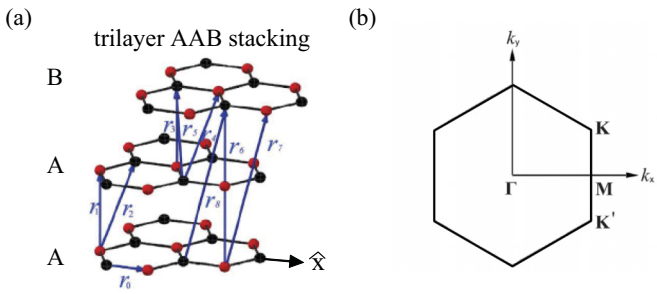

FIG. 1. The geometric structure of the trilayer AAB-stacked graphene in the presence of various intralayer and interlayer hopping integrals and its first Brillouin zone.

VASP calculations for the low-lying energy bands [15,16]. The band structure of the AAB-stacked TLG possesses three pairs of energy bands with oscillatory, sombrero-shaped and parabolic dispersions, and has a narrow band gap of <10 meV between oscillatory energy bands. Particularly, the acoustic plasmon mode in the long wavelength limit identifies the critical mechanism because of the large DOS of the oscillatory valence bands in the semiconducting pristine system or the free conduction electrons in the doping case. In this work, we conduct the first theoretical study of the doping effects on the Coulomb excitations and describe the related diversified phenomena.

Some theoretical works had presented the band structure, density of states, magnetic quantization, and magneto-optical properties for AAB-stacked TLG [15–17]. However, the significant studies dealing with the many-particle carrier excitations and deexcitations are absent, as far as we know. The complex possesses a very narrow band gap and unusual energy dispersions. Therefore, the electron-electron Coulomb interactions are expected to create rich and unusual excitation phenomena, such as the temperature- and doping-created low-frequency plasmons. The former characteristics have been identified from scanning tunneling spectroscopy (STS) measurements. It has also been observed that most pristine layered graphene exhibits semimetallic behavior, e.g., the AAA, ABA, and ABC stacking [17] and the bilayer twisted [18] and sliding systems [19]. However, the AAB-stacked TLG exhibits unusual optical vertical excitations at low energies, mainly owing to the unusual Van Hove singularities in the DOS [17]. Such energy bands induce magnetically quantized Landau levels, with noncrossing, crossing, and anticrossing B_z-dependent energy spectra [16], being quite different from those of monolayer, bilayer, and other kinds of TLG systems [17]. The lower-symmetry AAB-stacked TLG also has been predicted to have more complicated magneto-optical absorption spectra [17].

The electronic properties and Coulomb excitations of the lower-symmetry AAB TLG are investigated with the use of the tight-binding model in modified RPA. Specifically, the hopping integrals and electron-electron interactions from both interlayer and intralayer are taken into consideration simultaneously through the layer-dependent polarization functions. The low-lying energy bands mainly come from the $2p_z$ orbitals of six carbon atoms in a primitive unit cell, being examined with the first-principles calculations [14]. Three pairs of valence and conduction bands are identified to produce the unusual energy dispersions: the oscillatory, sombrero-shaped, and parabolic ones, as measured from E_F. The first two kinds of energy bands are predicted to yield Van Hove singularities in the density of states as square root asymmetric peaks. They could be viewed as quasi-one-dimensional (quasi-1D) parabolic bands. Moreover, the system has a very narrow energy gap (<10 meV). The single-particle excitations (SPEs) are expected to exhibit a lot of special structures because there are effectively the nine categories of the interband transitions, being related to the low-symmetry wave functions, for the nonvertical Coulomb excitations. The current study shows that a prominent plasmon peak, with low frequency (<0.2 eV), appears in the energy-loss function, which originated from the interband excitations of the first pair of energy bands. The dependence on transferred momentum and temperature is explored thoroughly. Furthermore, the similarities between 2D AAB-stacked TLG and 1D narrow-gap carbon nanotubes are discussed in detail. The effects of doping, which substantially changes the low-frequency plasmon modes, are also carefully studied. The number, intensity, frequency, and optical and acoustic modes of E_F-dependent plasmons and the various regions of intraband and interband electron-hole excitations are systematically investigated, which shows the disparate (momentum, frequency) phase diagrams with specific plasmon modes and distinct electron-hole boundaries. Finally, a detailed comparison among TLGs with different stackings is made, based on the single- and many-particle properties.

II. ENERGY-BAND STRUCTURE

The low-lying energy bands of the trilayer AAB stacking, which mainly originated from the $2p_z$ orbitals, were calculated within the tight-binding model. The resulting band structure is consistent with that from the first-principles method [14]. The first (last) two layers, as clearly shown in Fig. 1(a), are arranged in the AA (AB) stacking. In our notation, the A sublattice includes atoms (black spheres) with the same in-plane (x, y) coordinates and the B sublattice includes the others (red spheres). As a result, the atoms in the B sublattice of the third layer are projected onto the hexagonal centers of the other two layers and vice versa. The interlayer distance is $d = 3.37$ Å and the C–C bond length is $b = 1.42$ Å. There are six carbon atoms in a primitive unit cell, being similar to those in trilayer AAA, ABA, and ABC stackings. The low-energy electronic properties are characterized by the interactions between the $2p_z$ orbitals of the carbon atoms. The zero-field Hamiltonian, being built from the six tight-binding functions associated with the periodical $2p_z$ orbitals, is determined by the intralayer and the interlayer atomic interactions: γ_i. Because of lower symmetry for the stacking configuration, there exist ten types of hopping integrals for the matrix elements of the Hamiltonian. $\gamma_0 = -2.569$ eV represents the nearest-neighbor intralayer atomic interaction; $\gamma_1 = -0.263$ eV and $\gamma_2 = 0.32$ eV present the interlayer atomic interactions between the first and second layer; $\gamma_3 = -0.413$ eV, $\gamma_4 = -0.177$ eV, and $\gamma_5 = -0.319$ eV are associated with the interlayer atomic interactions between the second and third layer; $\gamma_6 = -0.013$ eV, $\gamma_7 = -0.0177$ eV, and $\gamma_8 = -0.0319$ eV relate to the interlayer atomic interactions

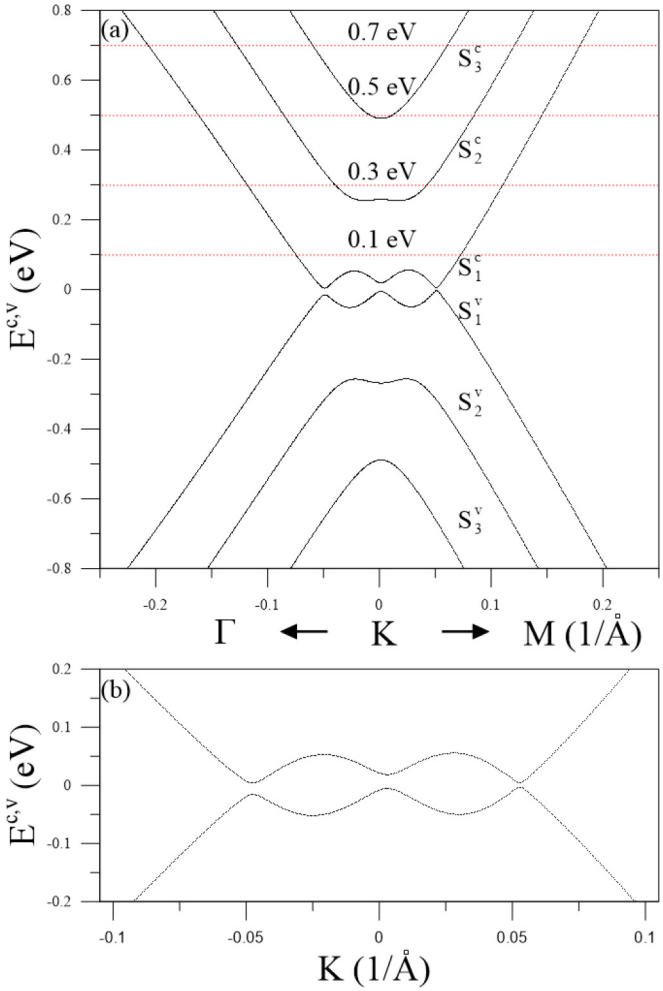

FIG. 2. (a) The low-lying valence and conduction bands for AAB-stacked TLG, with (b) a narrow gap of $E_g \sim 8$ meV arising from oscillatory energy bands.

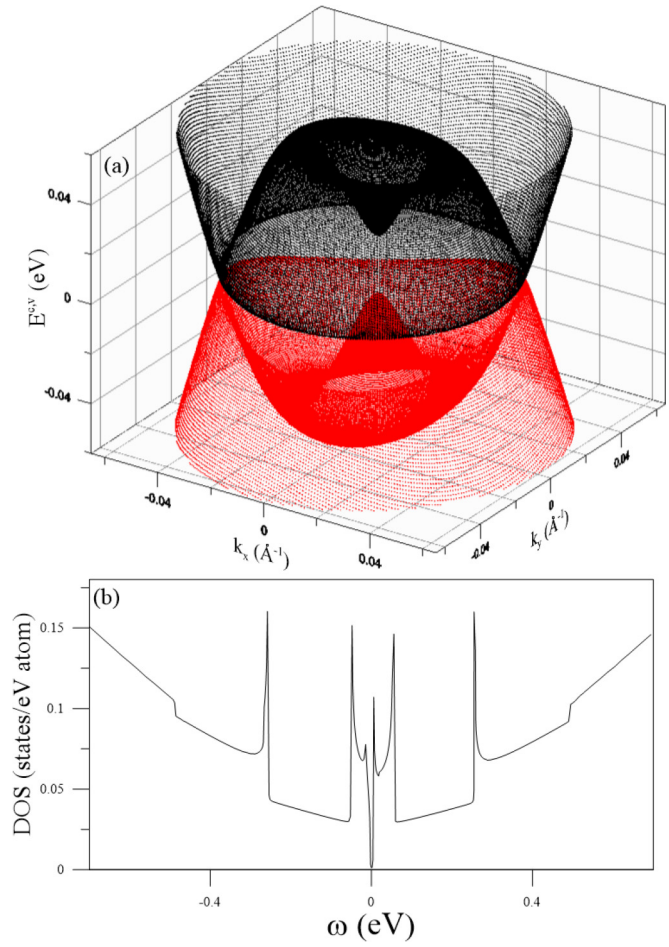

FIG. 3. (a) The 3D energy bands near E_F and (b) the low-energy density of states.

between the first and third layer; and $\gamma_9 = -0.012$ eV accounts for the difference between the chemical environments for A and B atoms. γ_1, γ_3, and γ_5 denote the vertical interlayer hopping integrals, while the others are nonvertical ones. We note that the above parameters are capable of characterizing the complex and unique energy bands of AAB-stacked TLG [Fig. 1(a)]. In addition, their magnitudes are comparable with those used in the other stacking systems, e.g., AAA [20], ABA [21], and ABC stackings [21].

Each pair of valence and conduction bands in AAB-stacked TLG, measured from the Fermi level, possess unique energy dispersions. These are the oscillatory, sombrero-shaped, and parabolic bands, as shown in Fig. 2. The first conduction band has an oscillatory band, with local minima of ∼4 meV at the K point and around ∼0.05/Å away from the K point, and local maxima of ∼60 meV around ∼0.025/Å away from the K point. With respect to $E_F = 0$, the first conduction band is almost symmetric with the first valence band, with corresponding opposite curvature. As a result, there exists a narrow energy gap of $E_g \sim 8$ meV and approximately three constant-energy contours at ±4 meV and ±60 meV. Such loops in the three-dimensional (3D) energy-wave-vector space could be effectively regarded as 1D parabolic bands [Fig. 3(a)]. Due to multifold degenerate states, the perturbation around $E_F = 0$ might miss some important features and the effective-mass model might become questionable to describe the low-energy properties. Our model keeps all essential features which are consistent with those from the first-principle calculations and becomes more suitable to study AAB-stacked TLG. As for the second pair of energy bands, their conduction band (valence band) has a sombrero-shaped energy dispersion with local energy minimum (maximum) and maximum (minimum), being located near 0.255 eV (−0.255 eV) and 0.26 eV (−0.26 eV), respectively. The energy difference between these two extreme points is very small (∼5 meV). The third pair of the energy bands consists of monotonic parabolic bands, for which the minimum (maximum) conduction (valence) state energy minimum is ∼0.49 (−0.49) eV. The above features of the low-lying energy bands are in agreement with those obtained from the first-principle calculations, indicating that the considered tight-binding model is appropriate and reliable [14]. We note that such energy dispersions also produce the unusual magnetic quantization and magneto-optical properties [15,16], such as the frequent intragroup and intergroup Landau-level anticrossings, and the intricate and rich magneto-optical absorption spectra, being never revealed in other stacking systems.

The energy dispersions have two kinds of Van Hove singularities in the density of states for AAB-stacked TLG, as shown in Fig. 3. The asymmetric square root peaks and the shoulder structures, respectively, arise from the constant-energy contours [Fig. 2(a)] and the band-edge states of the parabolic dispersions. Two pairs of asymmetric peak structures (Taiwanese temple structures) which are related to the first pair of oscillatory energy bands, are centered about E_F. The asymmetric peaks around ± 0.26 eV are due to the sombrero-shaped bands. The rich DOS structures leads to complex optical excitations, for which there are nine kinds of available vertical transitions arising from three pairs of valence and conduction bands. The number, frequency, intensity, and form of the optical absorption structures are predicted to be sensitive to the strength of an external electric field [17].

III. THEORY

The charge-density distribution is assumed to be uniform inside each layer. When an electron beam is injected into the AAB-stacked TLG, the π electrons on specific layers will screen the time-dependent external electrostatic potentials [$V_{ll'}(\mathbf{q})$, where l and l' are layer indices) via electron-electron interactions, leading to induced charge-density fluctuations and potentials. Within linear-response theory, the induced charge density is proportional to the effective Coulomb potentials [$V^{\rm eff}_{ll'}(\mathbf{q},\omega)$, where ω is the transferred frequency during charge screening]. By using the layer-based RPA, the effective Coulomb potentials are calculated by using Dyson's equation [22]:

$$\epsilon_0 V^{\rm eff}_{ll'}(\mathbf{q},\omega) = V_{ll'}(\mathbf{q}) + \sum_{m,m'} V_{lm}(\mathbf{q}) P^{(1)}_{m,m'}(\mathbf{q},\omega) V^{\rm eff}_{m'l'}(\mathbf{q},\omega), \tag{1}$$

where $\epsilon_0 = 2.4$ is the background dielectric constant. The external potential $V_{ll'}(\mathbf{q})$ is expressed as $v_q e^{-q|l-l'|I_c}$, where $v_q = 2\pi e^2/q$ is the 2D bare Coulomb potential of a 2D electron gas, and $I_c = 3.35$ Å is the layer distance [14]. The induced potential in the last term reveals the complex dynamic screening due to the intralayer and interlayer Coulomb interactions. The layer-dependent bare polarization function, being determined by energy bands and wave functions, is expressed as

$$\begin{aligned} P^{(1)}_{mm'}(\mathbf{q},\omega) = 2 \sum_k \sum_{n,n'} \sum_{h,h'=c,v} & \left(\sum_i u^{h}_{nmi}(\mathbf{k}) u^{h'*}_{n'm'i}(\mathbf{k}+\mathbf{q}) \right) \\ & \times \left(\sum_{i'} u^{h*}_{nm'i'}(\mathbf{k}) u^{h'}_{n'm'i'}(\mathbf{k}+\mathbf{q}) \right) \\ & \times \frac{f\left(E^h_n(\mathbf{k})\right) - f\left(E^{h'}_{n'}(\mathbf{k}+\mathbf{q})\right)}{E^h_n(\mathbf{k}) - E^{h'}_{n'}(\mathbf{k}+\mathbf{q}) + \hbar\omega + i\Gamma}. \end{aligned} \tag{2}$$

Here, u^h_{nmi} is the amplitude of the wave function on the ith sublattice of the mth layer, arising from the valence or conduction state ($h = c$ or v) of the nth energy band. $f(E^h_n(\mathbf{k})) = 1/\{1 + \exp\{[E^h_n(\mathbf{k}) - \mu(T)]/k_B T\}\}$ is the Fermi–Dirac distribution function. k_B, $\mu(T)$, and Γ stand for the Boltzmann constant, chemical potential, and the energy width due to various deexcitation mechanisms, respectively. The layer-dependent dielectric function is defined by

$$\epsilon_{ll'}(\mathbf{q},\omega) = \epsilon_0 \delta_{ll'} - \sum_m V_{lm}(\mathbf{q}) P^{(1)}_{m,l'}(\mathbf{q},\omega). \tag{3}$$

Making use of Eq. (3), one can express Eq. (1) as a linear tensor equation. The effective potential tensor is the inverse of the dielectric function tensor multiplied by the external potential tensor:

$$\mathbf{Im}[-1/\epsilon] \equiv \sum_l \mathbf{Im}\left[-V^{\rm eff}_{ll}(\mathbf{q},\omega)\right] \Big/ \left(\sum_{l,l'} V_{ll'}(\mathbf{q})/3 \right). \tag{4}$$

The dimensional energy-loss function is useful in understanding the inelastic-scattering probability of EELS measurements [22,23]. Equations (1)–(4), which include all the atomic and Coulomb interactions, are applicable to any layered graphene system.

IV. LOSS FUNCTION AND PLASMON EXCITATIONS

Different types of SPE channels and plasmon modes are now investigated in detail, especially for the frequency dependence of the electronic excitations on q and E_F. The predicted results could be verified by high-resolution EELS [24,25] and inelastic light scattering spectroscopy [26,27].

The unusual energy dispersions and Van Hove singularities lead to special structures in the SPE spectra. AAB-stacked TLG has six independent bare polarization functions (P_{11}, P_{22}, P_{33}, P_{12}, P_{13}, and P_{23}) because the equivalence between the top and bottom layer, which makes other kinds of well-stacked TLGs have four, is no longer maintained. As shown in Fig. 2(a), the band structure of pristine AAB-stacked TLG presents three pairs of energy bands, which create nine categories of interband transition channels ($i^v \rightarrow j^c$ for i and $j = 1, 2, 3$). The first pair of valence and conduction bands gives rise to two asymmetric peak structures in the lower-frequency polarization functions at small q, e.g., P_{ij} at $\omega = 0.01$ and 0.12 eV for $q = 0.005/$Å (black curves), and $\omega = 0.015$ and 0.12 eV for $q = 0.01/$Å (red curves) in Figs. 4 and 5. The real and imaginary parts, respectively, show a pair asymmetric peak structures and the square root divergent peak, directly reflecting the Kramers–Kronig relations. Notice that the Coulomb excitations belong to the nonvertical transitions. However, the transitions from the valence-band edge states to the conduction-band edge states could survive under small q. With increasing excitation frequency, the special structures occur in the range of 0.2 eV $< \omega <$ 0.4 eV without specific form. Such composite structures are associated with the large joint density of states from the band-edge states of the first oscillatory valence band and the second sombrero-shaped conduction band, and from the second sombrero-shaped valence band and the first oscillatory conduction band. The second pair of shallow sombrero-shaped energy bands only induce a square root peak (a pair of asymmetric structures) in Im[P_{ij}] (Re[P_{ij}]) within the range of 0.4 eV $< \omega <$ 0.6 eV. The second (third) valence states could also be excited to the third (second) conduction bands, where the band-edge states near the K point might lead to the special structures at 0.6 eV $< \omega <$ 0.8 eV. Finally, the third pairs of parabolic

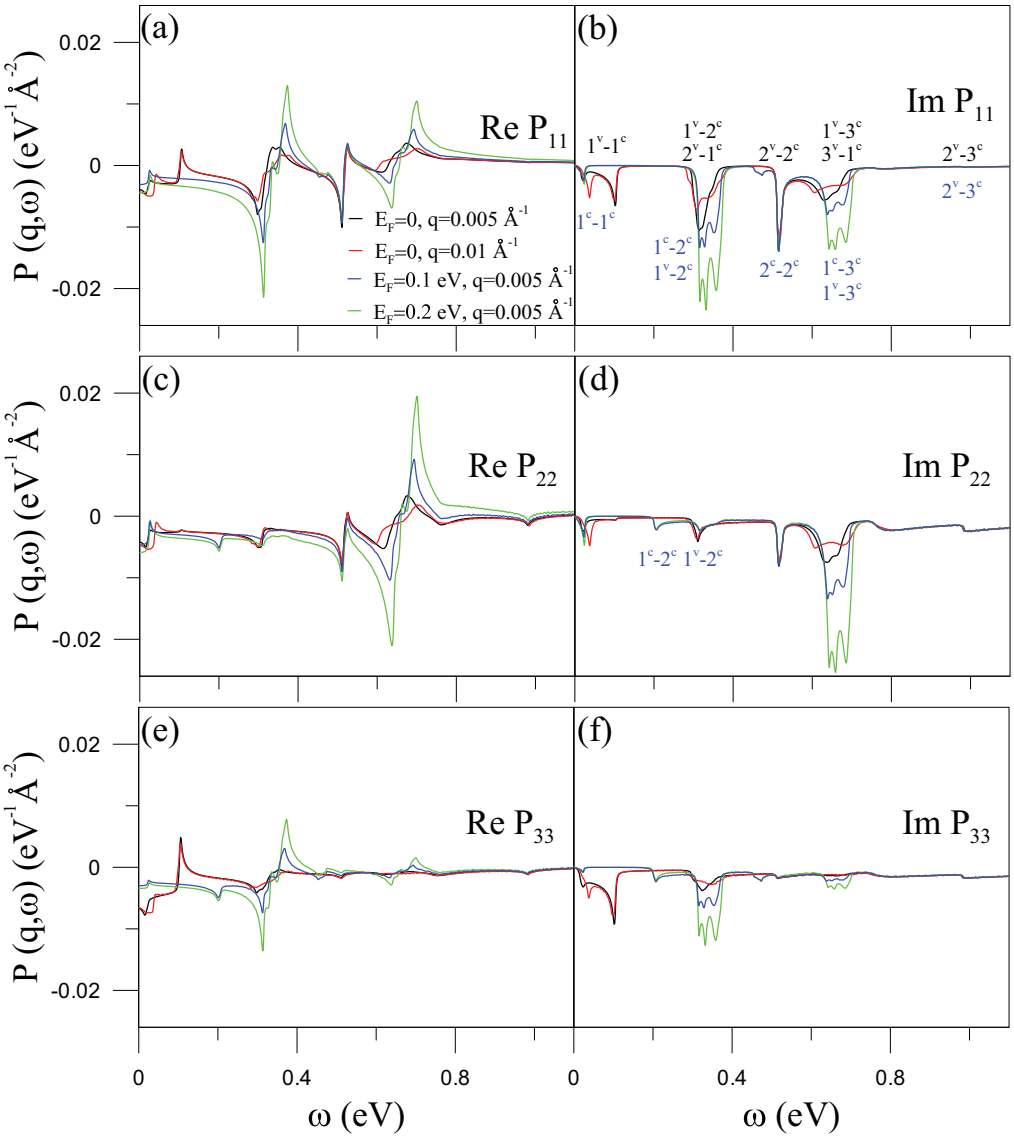

FIG. 4. The bare polarization functions for AAB-stacked TLG for chosen E_F and $\mathbf{q}$: (a) Re$[P_{11}]$, (b) Im$[P_{11}]$, (c) Re$[P_{22}]$, (d) Im$[P_{22}]$, (e) Re$[P_{33}]$, and (f) Im$[P_{33}]$.

bands show shoulder structure in Im$[P_{ij}]$ and the logarithmically symmetric peak in Re$[P_{ij}]$.

The energy-loss spectra of the undoped trilayer AAB stacking can exhibit a prominent peak, illustrating the dominating band-structure effect. The plasmon frequency lies in the range of 0.145 to 0.22 eV for the momentum range of $q = 0.005$–$0.02/\text{Å}$, as shown in Fig. 6(a). The intensity and frequency decreases and grows, respectively, as q is increased. This strong plasmon mode is related to the interband transitions of the first pair of the oscillatory energy bands [Fig. 2(b)], which directly reflects the Van Hove singularities nearest to E_F. The low-frequency plasmon peak is prominent because the frequency is not higher than the threshold for the Landau damping, which corresponds to the interband excitations of $1^v \to 2^c$ and $2^v \to 1^c$. Other low-intensity plasmon peaks could be observed in the screened response functions, e.g., in the inset of Fig. 6(a), the 0.32–0.38 eV peaks arising from the interband couplings between the first (second) valence band and the second (first) conduction band. On the other side, the low-frequency collective excitations are revealed with the significant peaks in narrow-gap carbon nanotubes [28,29]. While free electrons and holes cannot survive in these two systems, the creation of low-frequency prominent plasmon modes is attributed to the 2D oscillatory bands and the 1D parabolic bands, respectively, because of large DOS and the dimension- and wave-function-dependent strong Coulomb interactions in the long-wavelength limit. Furthermore, the energy-loss spectra at finite temperature ($T = 300$ K) is also studied in Fig. 6(a). Because of free carriers induced by thermal fluctuation, the plasmons from the intraband contribution cause damping, which would reduce the intensity and frequency at finite temperature.

Electron doping can drastically modify the collective excitations and the single-particle response functions (Im$[P_{ij}]$), as demonstrated in Figs. 4 and 5. For example, as for the low-doping case with $E_F = 0.1$ eV (the blue curves), certain interband excitation is forbidden by the Pauli exclusion principle, but new intraband excitation becomes allowed. The

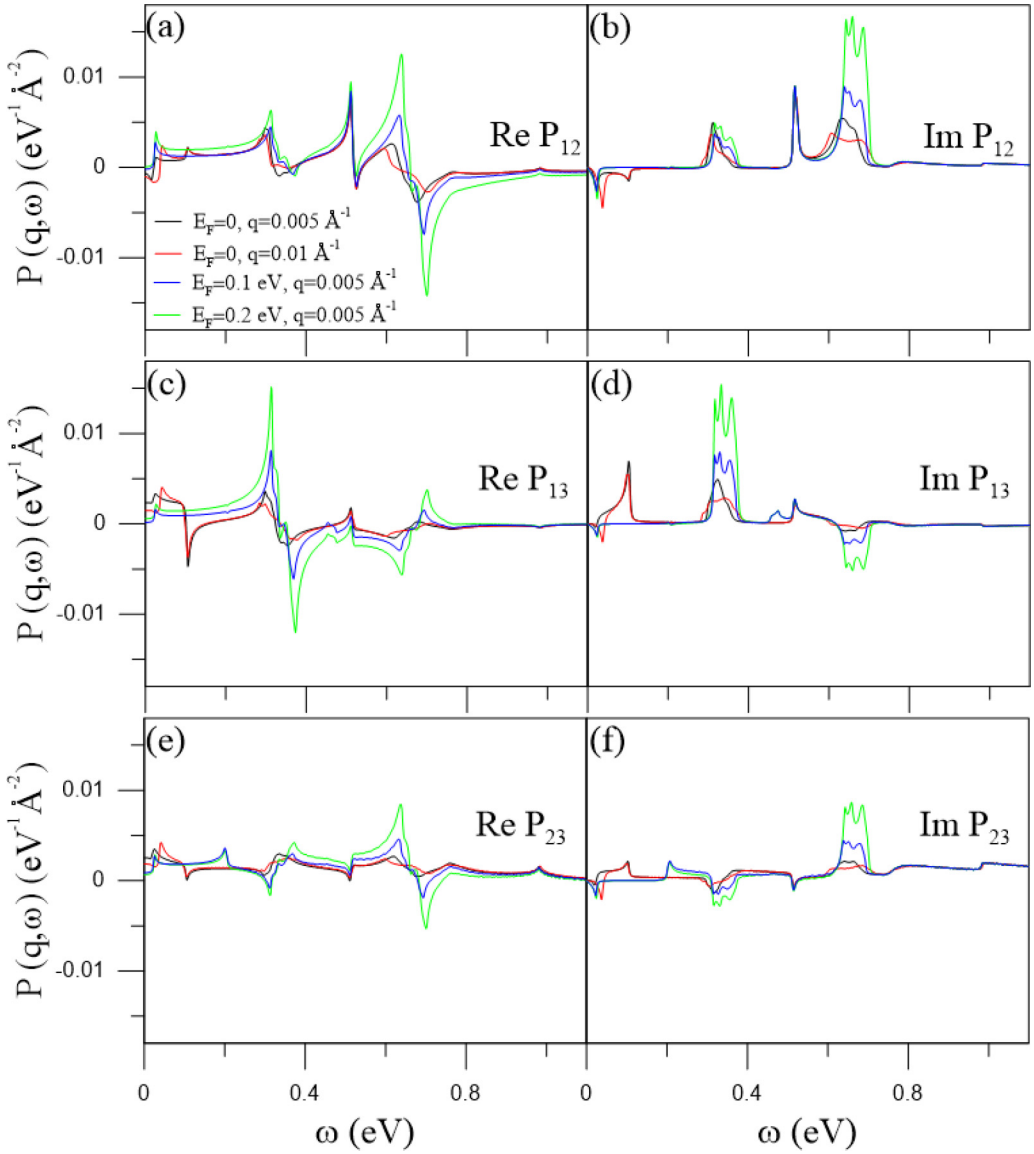

FIG. 5. Plots similar to those of Fig. 4 for (a) Re[P_{12}], (b) Im[P_{12}], (c) Re[P_{13}], (d) Im[P_{13}], (e) Re[P_{23}], and (f) Im[P_{23}].

low-frequency interband $1^v \rightarrow 1^c$ channel is replaced by the intraband $1^c \rightarrow 1^c$. The only special structure for small ω mainly comes from the Fermi momentum states. The linear energy dispersions near E_F lead to the asymmetric square root peak [30]. In the range of 0.2 eV $< \omega <$ 0.4 eV, the contribution is from both the original interband $1^v \rightarrow 2^c$ excitations and extra intraband $1^c \rightarrow 2^c$ excitations, which are mainly related to the band-edge states. With further increase of frequency, the identical structure at $\omega \sim 0.522$ eV is induced by the original interband $2^v \rightarrow 2^c$. For even higher frequencies, the $3^v \rightarrow 1^c$ channel is changed into the $1^c \rightarrow 3^c$ channel, while the $1^v \rightarrow 3^c$, $2^v \rightarrow 3^c$ and $3^v \rightarrow 3^c$ channels are unchanged. The variation of E_F can modify the SPEs, which result in the creation or destruction of the different plasmon modes. Notice that the threshold asymmetric structure at the lowest frequency can survive for any chosen E_F, which corresponds to the prominent acoustic plasmon peak.

The screened response functions (as shown in Fig. 6), which reveal the distinct collective excitations and the various Landau dampings, present rich and unique phenomena after electron doping. For lower doping with $E_F = 0.1$ [Fig. 6(b)], the frequency and intensity of the first plasmon peak are slightly reduced for the same q, compared with those for the pristine case $E_F = 0$ [Fig. 6(a)]. The peak for doping case corresponds to the Fermi momentum states, while that for zero doping is due to the valence-band edge states. The collective oscillations of charge carriers mainly come from the free conduction electrons and the valence electrons in the first pair of oscillatory energy bands. The plasmon is very sensitive to the direction of **q**, e.g., the great reduction in the strength and frequency of the low-frequency plasmon due to the significant interband Landau dampings [Fig. 6(c)]. Furthermore, the observable plasmons at higher frequencies, which are located in the range of 0.2eV $< \omega <$ 0.4 eV [see insets in Figs. 6(b) and 6(c)] are due to two distinct modes, the $1^v \rightarrow 2^c$ and $1^c \rightarrow 2^c$ channels. However, there is one interband plasmon peak for the undoped case [the inset in Fig. 6(a)] because of the similar excitation frequencies for

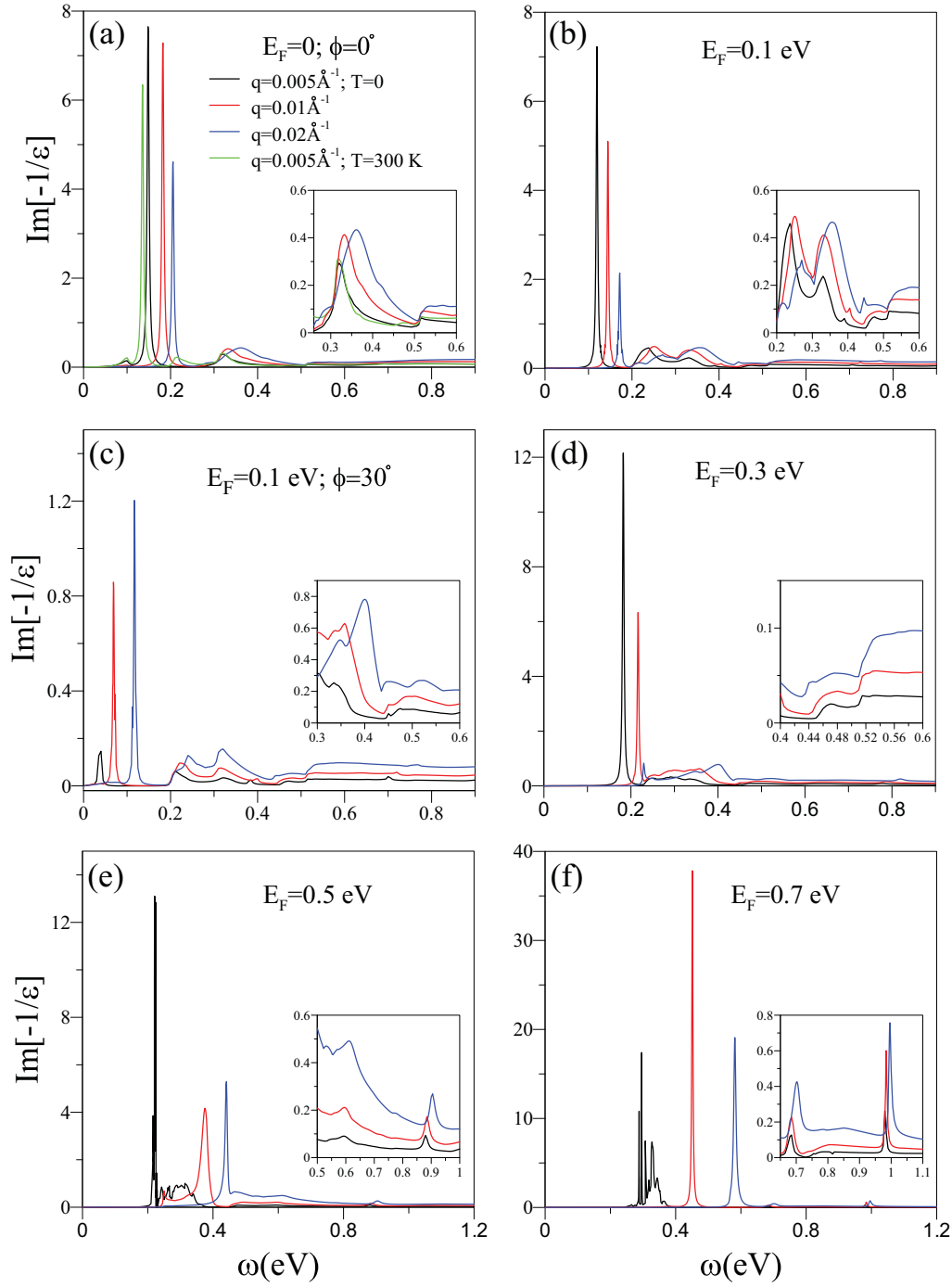

FIG. 6. The energy-loss functions for the chosen q and direction $\phi = 0^\circ$ when (a) $E_F = 0$, (b) 0.1, (d) 0.3, (e) 0.5, and (f) 0.7 eV. Panel (c) shows the results at $\phi = 30^\circ$ and $E_F = 0.1$ eV. The insets show the detail of structures for higher frequency, covering one or two optical plasmon modes.

the $1^v \to 2^c$ and $2^v \to 1^c$ channels. For larger E_F [e.g., $E_F = 0.3$ eV in Fig. 6(d)], there are more occupied states (free electrons) arising from the first and second conduction bands, so that two intraband excitation channels, the $1^c \to 1^c$ and $2^c \to 2^c$ channels, would enhance the bare and screened response functions. Consequently, the first plasmon mode has an enhanced frequency and strength. Similar excitation phenomena appear for even higher E_F, such as $E_F = 0.5$ eV [Fig. 6(e)] and 0.7 eV [Fig. 6(f)], crossing the third conduction band [Fig. 2(a)]. The energy-loss spectra clearly display drastic changes in the number, frequency, and intensity of the higher-frequency plasmon peaks for variations of E_F (see insets in Fig. 6).

The (momentum, frequency) phase diagrams are diversified by increasing the doping density, as shown in Fig. 7. The single-particle regions are enriched by doping. For the pristine system at zero temperature, the nine available interband excitations yield well-defined boundaries [Fig. 7(a)],

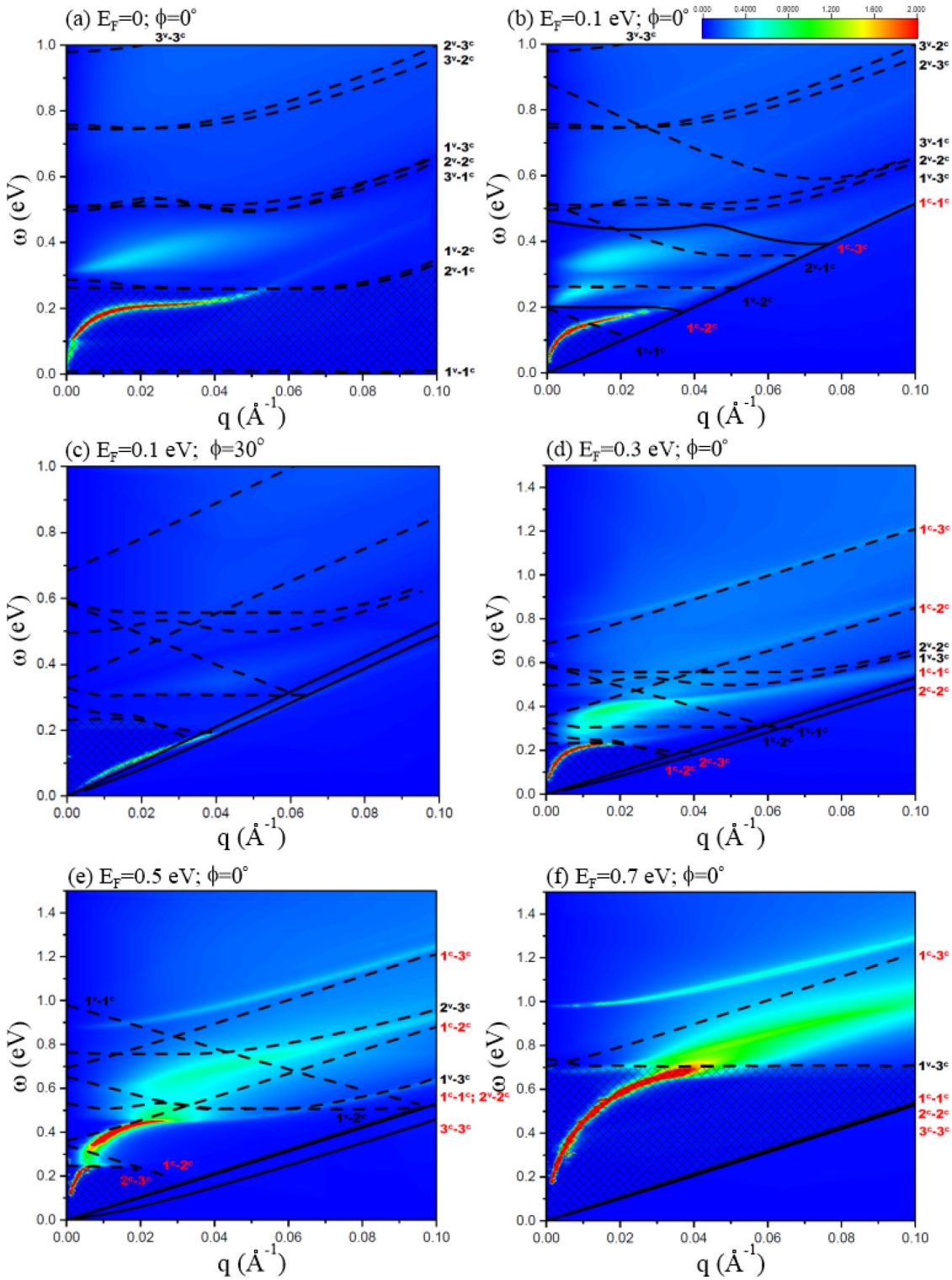

FIG. 7. The (momentum, frequency) phase diagrams of the trilayer AAB stacking under the various Fermi levels: (a) [$E_F = 0$, $\phi = 0°$], (b) [$E_F = 0.1$ eV, $\phi = 0°$], (c) [$E_F = 0.1$ eV, $\phi = 30°$], (d) [$E_F = 0.3$ eV, $\phi = 0°$], (e) [$E_F = 0.5$ eV, $\phi = 0°$], and (f) [$E_F = 0.7$ eV, $\phi = 0°$]. The region without the electron-hole excitations is indicated by the crosses.

being characterized mainly by the band-edge states (Fig. 2). Generally, the whole phase space is almost full of the electron-hole excitations. The specific region of the small q and ω exhibit very weak electron-hole excitations [the lower left-hand corner in Fig. 7(a)]. Similar behavior is revealed in the doped case, without the Landau dampings in the specific region [the crossed regions under $E_F \neq 0$ in Figs. 7(b)–7(f)]. The original boundaries are drastically modified by finite doping when the final Coulomb scattering states are associated with the partially occupied conduction energy bands, e.g.,

$E_F = 0.1$ eV [Fig. 7(b)], 0.3 eV [Figs. 7(c) and 7(d)], 0.5 eV [Fig. 7(e)], and 0.7 eV [Fig. 7(f)]. The interband excitation regions from valence bands of pristine TLG are greatly reduced by the increasing E_F, being beneficial for the existence of the low-frequency acoustic plasmon [Fig. 7(f)]. Furthermore, new excitation boundaries are created by the doping effects. For example, three kinds of extra electron-hole boundaries principally come from the $1^c \to 1^c$, $1^c \to 2^c$, and $1^c \to 3^c$ channels when E_F is between the first and second conduction energy bands, such as the SPE regions under $E_F = 0.1$ eV by the red notations.

An acoustic plasmon exists in any doping, with approximate $\sqrt{q}$ frequency dependence in the long-wavelength limit. In the pristine system, this mode is created by the valence electrons associated with a narrow energy gap, whereas it comes from all the conduction electrons related to the intraband excitations. The low-frequency plasmon in AAB-stacked TLG, which resembles the acoustic mode for the 2D electron gas [23], further illustrates the critical mechanism due to the large valence DOS of the oscillatory band or the free conduction electrons [Fig. 2(a)]. However, the critical momentum q_c strongly depends on the Fermi level, since the higher-energy interband excitations are mainly determined by it. The low-frequency plasmon would disappear [Figs. 7(a)–7(d)] or merge with the optical plasmon mode [Figs. 7(e)–7(f)] after entering the interband electron-hole excitation region for $q > q_c$. A simple relation between q_c and E_F is not available because of the complicated nonvertical interband Coulomb excitations, such as, $q_c = 0.054$, 0.03, 0.02, 0.04, and ~0.1 Å^{-1}, respectively, corresponding to $E_F = 0$, 0.1, 0.3, 0.5, and 0.7 eV. This plasmon mode is very prominent for the pristine and high-E_F cases [Figs. 7(a) and 7(f)], and it is relatively easy to measure the low-frequency collective excitations. The energy-loss spectra may yield one or two undamped modes, sensitive to E_F. One or two optical modes, respectively, correspond to ($E_F = 0$; 0.3 eV) and ($E_F = 0.1$ eV, 0.5 eV; 0.7 eV). In addition, the strongly hybridized optical plasmon modes might survive for a certain range of E_F, e.g., those within $E_F \sim 0.3$–0.5 eV [Figs. 7(c)–7(e)]. The optical plasmon in the pristine system is due to the interband $1^v \to 2^c$ and $1^v \to 2^c$ excitations. On the other hand, the diverse critical mechanisms, being sensitive to E_F, are revealed for two distinct optical modes for the doped cases. For example, when $E_F = 0.1$ eV ($E_F = 0.7$ eV), the second and third plasmons, with frequencies higher than 0.2 and 0.3 eV (0.65 and 0.95 eV), are dominated by the interband $1^c \to 2^c$ and $1^v \to 2^c$ excitations, as for the $1^v \to 3^c$ excitations at small transferred momenta. In general, two optical plasmons are closely related to the multi-interband excitation channels [Figs. 7(b)–7(f)].

The significant differences encompassed by the distinct trilayer stacking arrangements are worthy of a detailed comparison. Clearly, the AAB, AAA, ABA, and ABC stackings exhibit rich and unique Coulomb excitations, certainly illustrating the geometry-diversified phenomena [22,31–33]. From the calculated bare and screened response functions, different geometric symmetries, which have various interlayer hopping integrals, strongly affect the low-lying energy bands and thus the single-particle and collective excitations in the frequency range below ~1 eV. Evidently, the electron-hole excitation boundaries and regions are related to the band-edge states with the Van Hove singularities and the Fermi-momentum states, being sensitive to the stacking-generated energy dispersions. As a result, the electronic excitations are quite different among four kinds of stacking configurations. Concerning pristine ABC (AAA) stacking, the first pair of valence and conduction bands around E_F (the two pairs of Dirac cones below and above E_F) can create a strong special structure in the bare polarizability and a prominent peak in the energy-loss spectrum at low frequency. The low-frequency acoustic plasmon results from the valence states with the large DOS in AAB-stacking (narrow-gap) and ABC-stacking (gapless) [31] systems, or from the free electrons and holes in AAA TLG [32,33]. The first one and the latter two, respectively, display linear and square-root plasmon dispersions. On the other hand, it becomes challenging to observe this plasmon in the ABA stacking, mainly owing to low DOS from the valence-band edge states [34]. Such low-frequency plasmons can survive in any doped graphene, since they are induced by all the free carriers. There exist dramatic transformations in the available low-frequency excitation channels with gradually increasing doping. In general, the frequency and intensity of plasmons do not present an analytic dependence on E_F, except AAA-stacked TLG for low doping [32]. This is because AAB- and ABC-stacked TLGs have strong competition between the low-frequency interband excitations related to the valence-band edge states and the intraband excitations associated with the conduction electrons (the opposite variations of free electrons and holes in AAA stacking). Regarding the higher-frequency collective excitations, all the pristine AAB, ABA, and ABC stackings show one detectable optical mode arising from the most significant interband excitations. No optical plasmons are obtained in the undoped ABA stacking. Specifically, there are one or two optical modes in any doped system, being enriched by a lot of interband excitations due to the valence and conduction electrons. Many kinds of SPE channels and plasmon modes have been explored in detail, especially the strong dependence of the electronic excitations on the magnitude of q and E_F. It should be possible for the predicted results to be verified by high-resolution EELS [24,25] and inelastic light scattering spectroscopy [1–3,26,27].

V. CONCLUDING REMARKS

We have demonstrated that AAB-stacked TLG exhibit unique electronic properties, leading to diverse Coulomb excitations. The lower stacking symmetry leads to three pairs of unusual energy dispersions, i.e., the oscillatory, sombrero-shaped, and parabolic bands. The first two possess large and special Van Hove singularities, especially for the first pair nearest to the Fermi level. Consequently, for pristine systems, there are nine categories of valence-band to conduction-band transitions. The special structures in the bare response functions cover the square root asymmetric peaks and the shoulder structures (the pairs of antisymmetric prominent peaks and logarithmically symmetric peaks) in the imaginary (real) part. The threshold channel, $1^c \to 1^c$, can create significant SPEs and strong collective excitations. The low-frequency acoustic plasmon, being characterized by the pronounced peak in the

energy-loss spectrum, is due to the large DOS in the oscillatory valence and conduction bands and the narrow energy gap. Similar plasmon modes can be excited in a narrow-gap carbon nanotube [28,29]. The critical mechanism for the creation of this plasmon is thoroughly transformed into all the intraband conduction-band excitations, for which the effective channels and the critical transferred momenta strongly depend on the Fermi level.

After doping, the interband particle-hole excitation regions are drastically modified and the extra intraband excitations are generated by varying E_F. Moreover, one or two higher-frequency optical plasmon modes survive for various Fermi energies. They are closely related to the specific excitation channels or the strongly overlapped multichannels, being sensitive to the Fermi level and transferred momenta. There are important differences among the trilayer AAB, ABC, ABA, and AAA stackings, such as the boundaries of the various intraband and interband electron-hole excitations, and the mechanism, number, strength, frequency, and mode of the collective excitations. To fully explore the geometry-enriched Coulomb excitations, the above-mentioned theoretical predictions require experimental verifications.

ACKNOWLEDGMENTS

This work was supported in part by the National Science Council of Taiwan, the Republic of China, under Grant No. NSC 105-2112-M-006 -002 -MY3.

[1] J. Hermanson, Solid State Commun. **22**, 9 (1977).
[2] T. Ohta, Aaron Bostwick, J. L. McChesney, T. Seyller, K. Horn, and E. Rotenberg, Phys. Rev. Lett. **98**, 206802 (2007).
[3] W. Jin, P.-C. Yeh, N. Zaki, D. Zhang, J. T. Sadowski, A. Al-Mahboob, A. M. van der Zande, D. A. Chenet, J. I. Dadap, I. P. Herman, P. Sutter, J. Hone, and R. M. Osgood, Phys. Rev. Lett. **111**, 106801 (2013).
[4] H. Ibach and D. L. Mills, *Electron Energy Loss Spectroscopy and Surface Vibrations* (Academic Press, New York, 1982).
[5] A. Politano, G. Chiarello, V. Formoso, R. G. Agostino, and E. Colavita, Phys. Rev. B **74**, 081401 (2006).
[6] A. Politano and G. Chiarello, Gold Bull. (Geneva, Switz., 1968–1987) **42**, 195 (2009).
[7] A. Politano, V. Formoso, R. G. Agostino, E. Colavita, and G. Chiarello, Phys. Rev. B **76**, 233403 (2007).
[8] J. Lu, K. P. Loh, H. Huang, W. Chen, and A. T. S. Wee, Phys. Rev. B **80**, 113410 (2009).
[9] P. Xu, Y. R. Yang, D. Qi, S. D. Barber, J. K. Schoelz, M. L. Ackerman, L. Bellaiche, and P. M. Thibado, Phys. Rev. B **86**, 085428 (2012).
[10] W. T. Pong, J. Bendall, and C. Durkan, Surf. Sci. **601**, 498 (2007).
[11] L. B. Biedermann, M. L. Bolen, M. A. Capano, D. Zemlyanov, and R. G. Reifenberger, Phys. Rev. B **79**, 125411 (2009).
[12] Y. Que, W. Xiao, H. Chen, D. Wang, S. Du, and H. J. Gao, Appl. Phys. Lett. **107**, 263101 (2015).
[13] S. K. Asieh, S. Crampin, and A. Ilie, Appl. Phys. Lett. **102**, 163111 (2013).
[14] N. T. T. Tran, S. Y. Lin, C. Y. Lin, and M. F. Lin, *Geometric and Electronic Properties of Graphene-Related Systems: Chemical Bondings* (CRC Press, Boca Raton, 2017).
[15] T. N. Do, P. H. Shih, C. P. Chang, C. Y. Lin, and M. F. Lin, Phys. Chem. Chem. Phys. **18**, 17597 (2016).
[16] T. N. Do, C. Y. Lin, Y. P. Lin, P. H. Shih, and M. F. Lin, Carbon **94**, 619 (2015).
[17] C. Y. Lin, T. N. Do, Y. K. Huang, and M. F. Lin, *Optical Properties of Graphene in Magnetic and Electric fields, IOP Concise Physics. San Raefel, CA, USA* (Morgan & Claypool Publishers, 2017).
[18] E. Suárez Morell, J. D. Correa, P. Vargas, M. Pacheco, and Z. Barticevic, Phys. Rev. B **82**, 121407 (2010).
[19] Y. K. Huang, S. C. Chen, Y. H. Ho, C. Y. Lin, and M. F. Lin, Sci. Rep. **4**, 7509 (2014).
[20] J.-C. Charlier, J.-P. Michenaud, and X. Gonze, Phys. Rev. B **46**, 4531 (1992).
[21] J. C. Charlier, J. P. Michenaud, X. Gonze, and J. P. Vigneron, Phys. Rev. B **44**, 13237 (1991).
[22] J. H. Ho, C. L. Lu, C. C. Hwang, C. P. Chang, and M. F. Lin, Phys. Rev. B **74**, 085406 (2006).
[23] R. Egerton, *Electron Energy-Loss Spectroscopy in the Electron Microscope*, 3rd ed. (Springer, Berlin, 2011).
[24] P. Wachsmuth, R. Hambach, M. K. Kinyanjui, M. Guzzo, G. Benner, and U. Kaiser, Phys. Rev. B **88**, 075433 (2013).
[25] A. Politano, I. Radović, D. Borka, Z. L. Mišković, H. K. Yu, D. Farías, and G. Chiarello, Carbon **114**, 70 (2017).
[26] C. F. Chen, C. H. Park, B. W. Boudouris, J. Horng, B. Geng, C. Girit, A. Zettl, M. F. Crommie, R. A. Segalman, S. G. Louie, and F. Wang, Nature (London) **471**, 617 (2011).
[27] C. Kramberger, E. Einarsson, S. Huotari, T. Thurakitseree, S. Maruyama, M. Knupfer, and T. Pichler, Phys. Rev. B **81**, 205410 (2010).
[28] F. L. Shyu and M. F. Lin, J. Phys. Soc. Jpn. **71**, 1820 (2002).
[29] T. Pichler, M. Knupfer, M. S. Golden, J. Fink, A. Rinzler, and R. E. Smalley, Phys. Rev. Lett. **80**, 4729 (1998).
[30] Kenneth W.-K. Shung, Phys. Rev. B **34**, 979 (1986).
[31] C. Y. Lin, M. H. Lee, and M. F. Lin, Phys. Rev. B **98**, 041408(R) (2018).
[32] M. F. Lin, Y. C. Chuang, and J. Y. Wu, Phys. Rev. B **86**, 125434 (2012).
[33] R. Roldán, and L. Brey, Phys. Rev. B **88**, 115420 (2013).
[34] C. Y. Lin, M. C. Lin, J. Y. Wu, and M. F. Lin, arXiv:1803.10715.